SAND2007-6783C
08PFL-740

Large Eddy Simulation of Direct Injection Processes for Diesel and LTC Engine Applications

Tomasz G. Drozda and Joseph C. Oefelein
Sandia National Laboratories, Livermore, CA

ABSTRACT

Direct injection (DI) has proven to be a promising option in Diesel and low temperature combustion engines. In conventional Diesel and homogeneous charge compression ignition (HCCI) applications, DI lowers soot and NO_x production and improves fuel economy. In hydrogen fueled engines, DI provides the appropriate energy density required for high efficiency and low NO_x emissions. To realize the full benefit of DI, however, the effect of various injection parameters, such as injection timing, duration, pressure, and dilution, must be investigated and optimized under a range of engine operating conditions. In this work, we have developed a model for high-fidelity calculations of DI processes using the Large Eddy Simulation (LES) technique and an advanced property evaluation scheme. Calculations were performed using an idealized domain to establish a baseline level of validation. The baseline theoretical-numerical framework combines a general treatment of the governing conservation and state equations with state-of-the-art numerical algorithms and massively-parallel programming paradigm. This software enables both the canonical cases described here and in-cylinder calculations. Here we focus on high-pressure multi-port gas injectors designed for application in hydrogen-fueled IC-engines. This study was conducted in support of a larger effort to perform detailed in-cylinder LES calculations of companion optical engine experiments.

INTRODUCTION

Direct injection (DI) has proven to be of great importance for controlling combustion processes in internal combustion engines (ICE's). In Diesel engines, injected liquid fuel atomizes and evaporates while undergoing turbulent mixing with the oxidizer. These physical interactions, and in particular the level of mixing, affects the formation of soot and nitrogen oxides (NO_x). Similarly, homogeneous charge compression ignition (HCCI) technology has received much attention due to its high efficiency, low emissions combustion mechanism [1]. HCCI relies on autoignition of lean, or diluted, fuel-oxidizer mixtures at low flame temperatures [2] rather then on the propagation of high temperature flames. The former mode of combustion significantly reduces soot and NO_x production. But, when the equivalence ratio and temperature of the mixture decrease to below 0.15 and 1500K, respectively, combustion efficiency decreases [3]. Direct injection during the intake stroke or early compression stroke has been used as an effective way to control the mixture in a way that provides high efficiency and minimum emissions.

Recent research on hydrogen-fueled ICE's (H_2-ICE's) has demonstrated a potential to operate a transportation power plant with near-zero engine-out emissions [4, 5]. Unlike Diesel engines, H_2-ICE's are spark ignited (SI). The clean operation of the H_2-ICE's is largely due to the low flammability limit of hydrogen. This allows for stable engine operation at highly dilute low temperature conditions, which greatly reduces NO_x emissions. However, other properties of hydrogen make its combustion prone to knock, pre-ignition, and high levels of NO_x production. The later difficulty is mediated by diluting the fuel with EGR and using a three-way catalysts [6]. While spark knock is a property of the fuel, pre-ignition properties depend on the engine design and control strategy. In early research, the pre-ignition requirements of hydrogen cast doubt on its viability as a fuel. The most promising technique to control pre-ignition and boost power output is DI.

The primary challenge with DI H_2-ICE's is injection timing and enhancement of mixing. Typically, gaseous hydrogen (although cryogenic hydrogen can also be used [6]) is injected at intake valve closure (IVC). While this eliminates

the possibility of backfire, it also sets an upper limit on mixing time between the fuel and oxidizer before the mixture is ignited by the spark. In practice, the mixing time is lowered further by delaying the injection time with respect to IVC to avoid a partially premixed fuel-oxidizer mixture from contacting in-cylinder hot spots and pre-igniting. The start of injection (SOI), therefore, affects the level of unmixedness of the mixture at the time of spark ignition and has a direct impact on pollutant formation [7]. Delaying SOI decreases not only the mixing time but also the injection duration. Therefore, to realize the full benefit of DI while delivering a sufficient load, a large burden is placed on the injector to supply the fuel at increasingly high pressures and flow rates. Current injector technology limits engine operation from low to medium speeds [8]. The characteristics of several multi-port injectors have been investigated by Petersen [9, 10].

Due to the importance of DI on in-cylinder combustion processes, we have performed a high-fidelity Large Eddy Simulation (LES) of a canonical DI process. In LES, the large, energy containing scales of fluid motion are solved on a computational grid, while the small (more universal), subgrid-scales (SGS) are modeled. This allows predictions of unsteady dynamics of turbulent flow fields and in contrast to the Reynolds-Averaged Navier-Stokes (RANS) approximation, where both large and small scales of fluid motion are ensemble averaged. LES can be inherently more accurate, albeit more computationally expensive. The mathematical foundations of LES and its applicability in single and multiphase combustion are well established [11–16]. Several researchers have used, both, RANS and LES to perform DI studies [17–20].

As a step toward high-fidelity LES and systematic validation of our theoretical-numerical framework using available experiments, we have considered a series of canonical cases. One set are the jet penetration experiments performed in the constant-volume Diesel combustion chamber at the Combustion Research Facility (CRF) [21]. The second are the studies of high-pressure gas injectors designed for application in hydrogen-fueled IC-engines [9, 10]. Here we focus on the later.

EXPERIMENTAL DATA

Multi-port high-pressure hydrogen injector studies were conducted in a optically accessible chamber by Petersen and Ghandhi [9, 10]. Single, three, seven, nine, and thirteen port injectors were used. Single jet injection was achieved by blocking all but the central port of the seven port injector, or realigning one port of the three port injector with the chamber axis. Jet flow patterns were visualized using a Schlieren technique. The images were processed to determine the penetration length and angle. The pressure history during injection was also measured to determine the mass flow rate of the injected gas. Injection pressure, injected gas, chamber density, and chamber gas composition were varied to isolate the effects of pressure, density, compressibility, and ratio of specific heats. A summary of experimental conditions are provided in Tables. 1–3.

Table 1: Injection conditions considered in the experiments of Petersen [9].

No.	P_i[†] (bar)	ρ_i[‡] (kg/m^3)	Gas[§]
1	104	8.5	H_2
2	104	16.09	He
3	70	79.10	N_2
4	52	4.29	H_2
5	52	8.32	He
6	52	59.61	N_2
7	87.2		H_2, He
8	69.7		H_2, He
9	35.5		H_2, He
10	18.2		H_2, He
11	1.3-3.8[¶]		H_2, He

[†] Injection pressure
[‡] Injection gas density
[§] Injection gas composition
[¶] 1.3, 1.5, 1.9, 2.1, 2.4, 2.7, 3.2, 3.5, 3.8

Table 2: Chamber conditions considered in the experiments of Petersen [9].

No.	P_a[†] (bar)	ρ_a[‡] (kg/m^3)	Gas[§]
1	1	1.15	N_2
2	3.4	3.80	N_2
3	4.6	8.17	CO_2
4	7.2	12.82	CO_2
5	7.2	8.17	N_2

[†] Ambient chamber pressure
[‡] Ambient chamber gas density
[§] Chamber gas composition

Tables 1 and 2 show the range of conditions for the injection process and the chamber, respectively. Table 3 describes which multi-port hydrogen injectors were used in different cases. The numbers in this table denote the number of ports in an injector considered with corresponding injection and chamber conditions. The designations “all” and “none” indicate that all, or none, of the injectors were considered under corresponding injection and chamber conditions. These data were used to establish baseline validation of the model described below.

THEORETICAL–NUMERICAL FRAMEWORK

BASELINE FORMULATION. Results presented here were obtained using the theoretical-numerical framework developed by Oefelein [15, 16]. The numerical framework is appropriate for both DNS and LES applications and solves the fully coupled conservation equations of mass, momentum, total-energy and species. These equations can be expressed in conservative form as follows:

Table 3: Injector types studied under different injection and chamber conditions.

	Tab. 2				
Tab. 1	1	2	3	4	5
1	all[†]	all	3,7	all	all
2	all	all	7	all	all
3	all	all	none	none	all
4	all	all	3,7	all	all
5	all	all	7	all	all
6	all	all	none	none	all
7	3	3	none	none	3
8	3,7[‡]	3,7[‡]	none	none	3,7[‡]
9	3,7[‡]	3,7[‡]	none	none	3,7[‡]
10	3,7[‡]	3,7[‡]	none	none	3,7[‡]
11	1[§]	1	none	none	none

[†]All denotes the 3,7,9,and 13 port injectors

[‡]H_2 only

[§]Single jet is achieved by blocking all but the central port of seven port injector, or realigning one port of a three port injector with a chamber axis

- Mass:

$$\frac{\partial \rho}{\partial t} + \nabla \cdot (\rho \mathbf{u}) = 0. \tag{1}$$

- Momentum:

$$\frac{\partial}{\partial t}(\rho \mathbf{u}) + \nabla \cdot \left[\rho \mathbf{u} \otimes \mathbf{u} + \frac{p}{M^2}\mathbf{I}\right] = \nabla \cdot \tau, \tag{2}$$

where

$$\tau = \frac{\mu}{Re}\left[-\frac{2}{3}(\nabla \cdot \mathbf{u})\mathbf{I} + \left(\nabla \mathbf{u} + \nabla \mathbf{u}^T\right)\right]$$

represents the viscous stress tensor.

- Total Energy:

$$\frac{\partial}{\partial t}(\rho e_t) + \nabla \cdot [(\rho e_t + p)\mathbf{u}] = \nabla \cdot \left[\mathbf{q}_e + M^2(\tau \cdot \mathbf{u})\right], \tag{3}$$

where

$$\begin{aligned} e_t &= e + \frac{M^2}{2}\mathbf{u} \cdot \mathbf{u} \\ e &= \sum_{i=1}^{N} h_i Y_i - \frac{p}{\rho} \\ h_i &= h_{f_i}^{\circ} + \int_{p^\circ}^{p}\int_{T^\circ}^{T} C_{p_i}(T,p)dTdp \end{aligned}$$

represents the total internal energy, internal energy and enthalpy of the i^{th} species, respectively, and $\mathbf{q}_e$ the energy diffusion flux.

- Species:

$$\frac{\partial}{\partial t}(\rho Y_i) + \nabla \cdot (\rho Y_i \mathbf{u}) = \nabla \cdot \mathbf{q}_i + \dot{\omega}_i \qquad i = 1, \ldots, N-1, \tag{4}$$

where $\mathbf{q}_i$ and $\dot{\omega}_i$ represent the mass diffusion fluxes and the rate of production of the i^{th} species, respectively.

Equations (1) through (4), coupled with 1) an appropriate equation of state, 2) appropriate treatments of thermodynamic and transport properties, and 3) validated mixing and combining rules for the mixtures of interest accommodate the most general system of interest including cases where multicomponent and/or preferential diffusion processes are present. The viscous stress tensor is assumed to follow Stokes' hypothesis, and the heat release due to chemical reaction in Eq. (3) is accounted for in the description of the specific enthalpies, h_i, as given by the enthalpy of formation, $h_{f_i}^{\circ}$. The heat release rate can be represented equivalently, as a source term on the right hand side of Eq. (3), as the product of the enthalpy of formation and the local rate of production of all the species considered in the system. Using this representation, the source term and specific enthalpies would be defined as

$$\dot{Q}_e = -\sum_{i=1}^{N} \dot{\omega}_i h_{f_i}^{\circ}, \text{ and} \tag{5}$$

$$h_i = \int_{p^\circ}^{p}\int_{T^\circ}^{T} C_{p_i}(T,p)dTdp. \tag{6}$$

The theoretical formulation handles a generalized treatment of the equation of state, thermodynamics, transport processes, and chemical kinetics for the full multicomponent system. The numerical formulation treats the fully compressible conservation equations, but can be evaluated in the incompressible limit. Thus, incompressibility is treated as a limiting extreme of the more general compressible equation set given above. A unique dual-time multistage scheme is employed with a generalized preconditioning methodology that optimally treats convective, diffusive, geometric, and source term anomalies in a unified manner. The spatial scheme employs a staggered methodology in generalized curvilinear coordinates. The algorithm has been optimized to provide excellent parallel scalability attributes using a multiblock domain decomposition with distributed-memory message-passing.

FILTERED CONSERVATION EQUATIONS. For LES applications, the filtered version of Eqs. (1)–(4) are solved. These equations are given, respectively, as:

$$\frac{\partial \overline{\rho}}{\partial t} + \nabla \cdot (\overline{\rho}\tilde{\mathbf{u}}) = 0, \tag{7}$$

$$\frac{\partial}{\partial t}(\overline{\rho}\tilde{\mathbf{u}}) + \nabla \cdot \left[\left(\overline{\rho}\tilde{\mathbf{u}} \otimes \tilde{\mathbf{u}} + \frac{\mathcal{P}}{M^2}\mathbf{I}\right)\right] = \nabla \cdot \vec{\vec{\mathcal{T}}}, \tag{8}$$

$$\begin{aligned} \frac{\partial}{\partial t}(\overline{\rho}\tilde{e}_t) &+ \nabla \cdot [(\overline{\rho}\tilde{e}_t + \mathcal{P})\tilde{\mathbf{u}}] \\ &= \nabla \cdot \left[\left(\vec{\mathcal{Q}}_e + M^2(\vec{\vec{\mathcal{T}}} \cdot \tilde{\mathbf{u}})\right)\right] + \overline{\dot{Q}}_e, \end{aligned} \tag{9}$$

$$\frac{\partial}{\partial t}(\overline{\rho}\tilde{Y}_i) + \nabla \cdot (\overline{\rho}\tilde{Y}_i\tilde{\mathbf{u}}) = \nabla \cdot \vec{\mathcal{S}}_i + \overline{\dot{\omega}}_i. \tag{10}$$

The terms $\mathcal{P}$, $\vec{\vec{\mathcal{T}}}$, $\vec{\mathcal{Q}}_e$ and $\vec{\mathcal{S}}_i$ represent respective composite (i.e., molecular plus *sgs*) stresses and fluxes. The terms $\overline{\dot{Q}}_e$ and $\overline{\dot{\omega}}_i$ represent the filtered energy and species source terms.

SUBGRID-SCALE CLOSURE. The subgrid-scale closure is obtained using the "mixed" dynamic Smagorinsky model by combining the models proposed by Erlebacher, Hussaini, Speziale and Zang [22] and Speziale [23] with the dynamic modeling procedure [24–28]. The composite stresses and fluxes in Eqs. (7)–(10) are given as

$$\vec{\vec{\mathcal{T}}} = (\mu_t+\mu)\frac{1}{Re}\left[-\frac{2}{3}(\nabla\cdot\tilde{\mathbf{u}})\mathbf{I}+\left(\nabla\tilde{\mathbf{u}}+\nabla\tilde{\mathbf{u}}^T\right)\right] -\overline{\rho}\left(\widetilde{\tilde{\mathbf{u}}\otimes\tilde{\mathbf{u}}}-\tilde{\tilde{\mathbf{u}}}\otimes\tilde{\tilde{\mathbf{u}}}\right), \quad (11)$$

$$\vec{\mathcal{Q}}_e = \left(\frac{\mu_t}{Pr_t}+\frac{\mu}{Pr}\right)\frac{1}{Re}\nabla\tilde{h}+\sum_{i=1}^{N}\tilde{h}_i\vec{\mathcal{S}}_i -\overline{\rho}\left(\widetilde{\tilde{h}\tilde{\mathbf{u}}}-\tilde{\tilde{h}}\tilde{\tilde{\mathbf{u}}}\right), \text{ and} \quad (12)$$

$$\vec{\mathcal{S}}_i = \left(\frac{\mu_t}{Sc_{t_i}}+\frac{\mu}{Sc_i}\right)\frac{1}{Re}\nabla\tilde{Y}_i-\overline{\rho}\left(\widetilde{\tilde{Y}_i\tilde{\mathbf{u}}}-\tilde{\tilde{Y}}_i\tilde{\tilde{\mathbf{u}}}\right). \quad (13)$$

The term μ_t represents the *sgs* eddy viscosity, given by

$$\mu_t = \overline{\rho}C_R\Delta^2\Pi_{\tilde{\mathbf{S}}}^{\frac{1}{2}}, \quad (14)$$

where

$$\Pi_{\tilde{\mathbf{S}}} = \tilde{\mathbf{S}}:\tilde{\mathbf{S}}, \text{ and } \tilde{\mathbf{S}} = \frac{1}{2}\left(\nabla\tilde{\mathbf{u}}+\nabla\tilde{\mathbf{u}}^T\right). \quad (15)$$

The terms C_R, Pr_t, and Sc_{t_i} represent the Smagorinsky, *sgs*-Prandtl and *sgs*-Schmidt numbers and are evaluated dynamically as functions of space and time. The overall model includes the Leonard and cross-term stresses and provides a Favre averaged generalization of the Smagorinsky eddy viscosity model [29] coupled with gradient diffusion models that simulate subgrid-scale mass and energy transport processes.

THERMODYNAMIC AND TRANSPORT PROPERTIES. The property evaluation scheme is designed to account for thermodynamic nonidealities and transport anomalies over a wide range of pressures and temperatures. An example of typically encountered thermodynamic regimes is shown in Fig. 1. The scheme is comprehensive and intricate, thus only a skeletal description can be given here. The extended corresponding states model [30, 31] is employed with a cubic equation of state. In past studies, modified versions of both the Benedict-Webb-Rubin *(BWR)* equation of state and cubic equations of state have been used to evaluate the *p-v-T* behavior of the inherent dense multicomponent mixtures. Use of modified *BWR* equations of state in conjunction with the extended

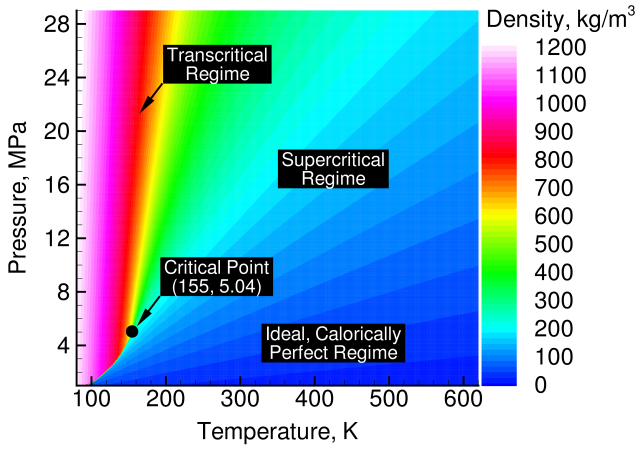

Figure 1: Thermodynamic regimes of interest using oxygen as an example.

corresponding states principle has been shown to provide consistently accurate results over the widest range of pressures, temperatures and mixture states, especially at near-critical conditions. A major disadvantage of *BWR* equations, however, is that they are not computationally efficient.

Cubic equations of state can be less accurate, especially for mixtures at near-critical or saturated conditions, but are computationally efficient. Experience has shown that both the Soave-Redlich-Kwong *(SRK)* and Peng-Robinson *(PR)* equations, when used in conjunction with the corresponding states principle, can give accurate results over the range of pressures, temperatures and mixture states of interest in this study. The *SRK* coefficients are fit to vapor pressure data and are thus more suitable for conditions when the reduced temperature is less than one. The *PR* coefficients, on the other hand, are more suitable for conditions when the reduced temperature is greater than one. Here the *PR* equation of state was used exclusively. A summary of the cubic equations of state and recommended constants is given by Reid et al. [32, Chapter 3].

Having established an analytical representation for real mixture *p-v-T* behavior, the thermodynamic properties are obtained in two steps. First, respective component properties are combined at a fixed temperature using the extended corresponding states methodology outlined above to obtain the mixture state at a given reference pressure. A pressure correction is then applied using departure functions of the form given by Reid et al. [32, Chapter 5]. These functions are exact relations derived using the Maxwell relations (see VanWylen and Sonntag [33, Chapter 10], for example) and make full use of the real mixture *p-v-T* path dependencies dictated by the equation of state. Standard state properties are obtained using the databases developed by Gordon and McBride [34] and Kee et al. [35]. Chemical potentials and fugacity coefficients are obtained in a similar manner.

Table 4: Critical properties of hydrogen and nitrogen.

	H_2	N_2
$T_c\ (K)$[†]	33.19	126.192
$P_c\ (MPa)$[‡]	1.3150	3.3958
$\rho_c\ (kg/m^3)$[§]	30.12	313.300

[†]Critical temperature
[‡]Critical pressure
[§]Critical density

Molecular transport properties are evaluated in a manner analogous to the thermodynamic properties. Viscosity and thermal conductivity are obtained using the extended corresponding states methodologies developed by Ely and Hanley [36, 37]. The mass diffusion coefficients and thermal diffusion coefficients are obtained using the methodologies outlined by Bird et al. [38] and Hirschfelder et al. [39] in conjunction with the corresponding states methodology proposed by Takahashi [40].

RESULTS AND DISCUSSION

To validate the coupled theoretical-numerical framework and property evaluation scheme described above, we have performed a high-fidelity LES of a single port high-pressure gaseous hydrogen injector. The injector geometry and flow conditions corresponds to those of a three port injector of Petersen [9, 10]. The port orifice diameter is 0.8 mm. The hydrogen gas is injected at a pressure of 104 bar into an ambient nitrogen mixture at a pressure of 3.4 bar. These conditions correspond to case numbers 1 and 2 in Tables 1 and 2, respectively. The corresponding critical properties of hydrogen and nitrogen are shown in Table 4. The high-pressure of the injection process places it in the supercritical regime, as illustrated in Fig. 1.

A *priori* validation of the accuracy of our property evaluation procedure with available experimental data is shown in Fig. 2. The experimentally obtained density data of Vargaftik [41] is compared to density calculated using our scheme. The results are in excellent agreement with the experimental data. Figure 2 also shows the specific heat, dynamic viscosity and thermal conductivity of oxygen versus temperature over the same range of temperatures and pressures. It is important to note that the methods applied here are applicable to any arbitrary hydrocarbon mixture at typical conditions of interest in IC-engines.

The computational domain spans, axially, 10 injector orifice diameters into the injector port and 100 diameters downstream of the port exit. The radial extent of this domain is 40 diameters. The computational grid is carefully tailored to facilitate high-fidelity LES, both, inside the injector port and inside the chamber. The full three-dimensional grid contains approximately 3,000,000 cells. The injector orifice is included in the calculations, with stretching applied in the wall-normal direction such that the first cell from the wall was within a y^+ value of 1 and the first 16 cells within the interval $0 < y^+ < 30$. The transverse grid spacing was set such that Δx^+ and Δz^+ where approximately 50. No-slip boundary conditions were applied at the upper and lower walls.

The instantaneous shadowgraph obtained in the experiments of the three port hydrogen injector and several isocontours of the density field obtained from LES are shown in Fig. 3. This representative example shows the level of qualitative agreement obtained between the experimentally observed and simulated results.

To quantify the results, jet penetration measurements obtained from the LES are shown in Fig. 4. The penetration length was calculated by measuring the distance from the jet's exit to a location along the centerline, where the mass fraction of hydrogen fell below a value of 3% of the maximum. The LES results are in good agreement with the experimental data. Calculations of the entire set of injectors are in progress.

CONCLUSIONS

A high-fidelity LES of a high-pressure hydrogen direct injection process has been conducted. To account for the relevant physical processes, a novel thermodynamic and transport property evaluation scheme has been implemented and a basline level of validation has been established. This scheme accounts for thermodynamic nonidealities and transport anomalies over a wide range of pressures and temperatures. In addition to the simple binary system considered here, the overall scheme is applicable to a wide variety of hydrocarbon mixtures.

The simulation results were compared to the experiments of Petersen and Ghandhi [9, 10]. Good qualitative and quantitiative agreement was obtained by comparing both shadowgraph results and the jet penetration data acquired in the experiment. The LES resolved turbulence structures are also in good qualitative agreement with those observed experimentally. The current work provides a baseline level of validation. Ongoing extensions include performing a systematic study of of the set of multi-port injectors studied by Petersen and Ghandhi. These results will be included in the final paper along with preliminary results from a parallel effort focused on hydrocarbon injection processes. The objective is to develop a validated capability for application in full optical engine geometries.

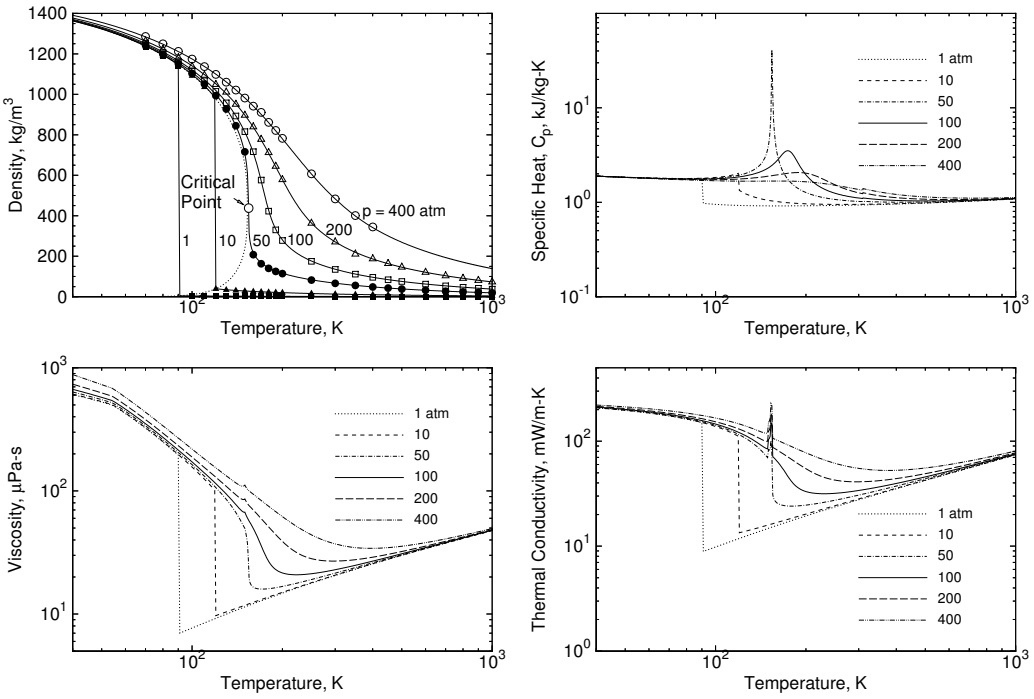

Figure 2: Density (compared with experimental data points obtained by Vargaftik [41]), specific heat, viscosity, and thermal conductivity versus temperature over the interval $40 \leq T \leq 1000$ and pressures of 1, 10, 50, 100, 200, and 400 atmospheres for pure oxygen.

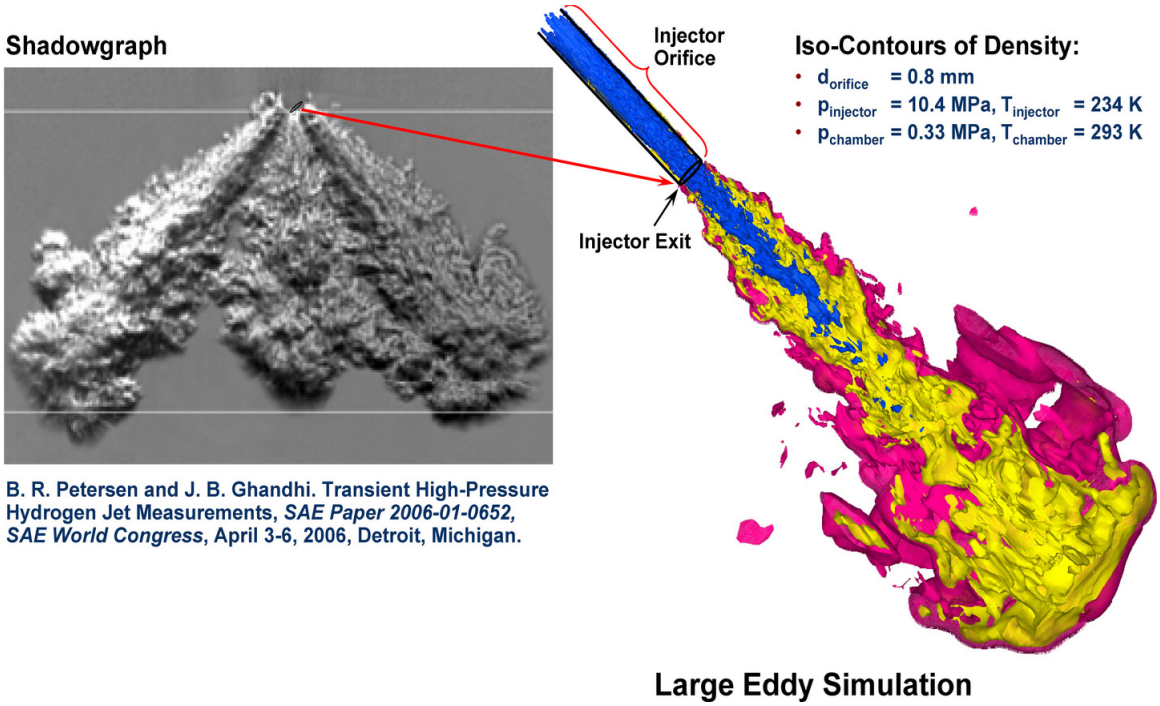

Figure 3: LES of the instantaneous jet structure compared to the shadowgraph results of Petersen *et al.* [9, 10] at the same instant in time.

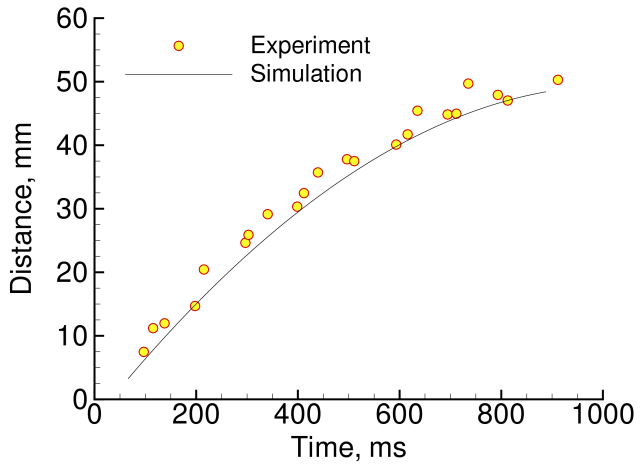

Figure 4: Jet penetration length as a function of time compared to the experimental measurements of Petersen *et al.* [9, 10].

REFERENCES

[1] F. Zhao, editor. *Homogeneous Charge Compression Ignition (HCCI) Engines: Key Research and Development Issues*. SAE International, March 2003.

[2] S. Kook, C. Bae, P. Miles, D. Choi, and L. M. Pickett. The influence of charge dilution and injection timing on low-temperature diesel combustion and emissions. In *Powertrain and Fluid Systems Conference and Exhibition*, volume 114 of *SAE Transactions*. SAE International, San Antonio, Texas, USA, October 2005. SAE Paper 2005-01-3837.

[3] L. M. Pickett. Low flame temperature limits for mixing-controlled diesel combustion. *Proc. Combust. Inst.*, 30(2):2727–2735, January 2005.

[4] L. M. Das. Hydrogen engines: A view of the past and a look into the future. *Int. J. Hydrogen Energy*, 15(6):425–443, 1990.

[5] H. Eichlseder, T. Wallner, R. Freymann, and J. Ringler. The potential of hydrogen internal combustion engines ina future mobility scenario. In *Future Transportation Technology Conference*, Costa Mesa, California, USA, June 2003. SAE, SAE International.

[6] C. M. White, R. R. Steeper, and A. E. Lutz. The hydrogen-fueled internal combustion engine: A technical review. *Int. J. Hydrogen Energy*, 31(10):1292–1305, August 2006.

[7] H. S. Homan, P. C. T. de Boer, and W. J. McLean. The effect of fuel injection on NOx emissions and undesirable combustion for hydrogen-fuelled piston engines. *Int. J. Hydrogen Energy*, 8(2):131–146, 1983.

[8] M. Berckmüller, H. Rottengruber, A. Eder, N. Brehm, G. Elsässer, G. Müller-Alander, and C. Schwarz. Potentials of a charged SI-hydrogen engine. In *Powertrain and Fluid Systems Conference and Exhibition*, Pittsburgh, Pennsylvania, USA, October 2003. SAE International. SAE Paper 2003-01-3210.

[9] B. R. Petersen. Transient high-pressure hydrogen jet measurements. Master of Science in Mechanical Engineering, University of Wisconsin-Madison, 2006.

[10] B. R. Petersen and J. B. Ghandhi. Transient high-pressure hydrogen jet measurements. In *Journal of Engines*, volume 115 of *SAE Transactions*. SAE International, Detroit, Michigan, USA, April 2006. SAE Paper 2006-01-0652.

[11] R. O. Fox. *Computational Models for Turbulent Reacting Flows*. Cambridge University Press, Cambridge, UK, 2003.

[12] L. C. Berselli, T. Iliescu, and W. J. Layton. *Mathematics of Large Eddy Simulation of Turbulent Flows*. Springer-Verlag, 2006.

[13] P. Sagaut. *Large Eddy Simulation of Incompressible Flows: An Introduction*. Springer-Verlag, third edition, 2006.

[14] H. Pitsch. Large-eddy simulation of turbulent combustion. *Annu. Rev. Fluid Mech.*, 38(1):453–482, 2006.

[15] J. C. Oefelein. Large eddy simulation of turbulent combustion processes in propulsion and power systems. *Prog. Aerosp. Sci.*, 42(1):2–37, January 2006.

[16] J. C. Oefelein, T. G. Drozda, and V. Sankaran. Large eddy simulation of turbulence-chemistry interactions in reacting flows. *J. Phys. Conf. Ser.*, 46:16–27, 2006.

[17] R. Jhavar and C. J. Rutland. Using large eddy simulations to study mixing effects in early injection diesel engine combustion. In *SAE 2006 World Congress*, Detroit, Michigan, USA, April 2006. SAE, SAE International. SAE Paper 2006-01-0871.

[18] T. Hori, J. Senda, T. Kuge, and H. G. Fujimoto. Simulation of non-evaporative and evaporative diesel spray in constant volume vessel by use of KIVALES. In *Powertrain and Fluid Systems Conference and Exhibition*, Toronto, Ontario, Canada, October 2006. SAE, SAE International. SAE Paper 2006-01-3334.

[19] T. Hori, T. Kuge, J. Senda, and H. Fujimoto. Three-dimensional analysis of diesel spray structure by use of large eddy simulation. In *JSAE Spring Conference*, Yokohama, Japan, May 2006. SAE, SAE International. SAE Paper 2006-08-0362.

[20] T. Hori, T. Kuge, J. Senda, and H. Fujimoto. Large eddy simulation of diesel spray combustion with eddy-dissipation model and CIP method by use of KIVALES. In *SAE 2007 World Congress*, Detroit, Michigan, USA, April 2007. SAE, SAE International. SAE Paper 2007-01-0247.

[21] L. Pickett. Engine Combustion Network. http://public.ca.sandia.gov/ecn/, September 2007.

[22] G. Erlebacher, M. Y. Hussaini, C. G. Speziale, and T. A. Zang. Toward the large eddy simulation of compressible turbulent flows. *Journal of Fluid Mechanics*, 238:155–185, 1992.

[23] C. G. Speziale. Galilean invariance of subgrid-scale stress models in the large-eddy simulation of turbulence. *J. Fluid Mech.*, 156:55–62, 1985.

[24] M. Germano, U. Piomelli, P. Moin, and W. H. Cabot. A dynamic subgrid-scale eddy viscosity model. *Physics of Fluids*, 3(7):1760–1765, 1991.

[25] P. Moin. Towards large eddy and direct numerical simulations of complex turbulent flows. *Comput. Method. Appl. M.*, 87:329–334, 1991.

[26] D. K. Lilly. A proposed modification of the Germano subgrid-scale closure method. *Phys. Fluids A*, 4(3):633–634, 1992.

[27] Y. Zang, R. L. Street, and J. R. Koseff. A dynamic mixed subgrid-scale model and its application to turbulent recirculating flows. *Physics of Fluids*, 5(12):3186–3195, 1993.

[28] B. Vreman, B. Geurts, and H. Kuerten. On the formulation of the dynamic mixed subgrid-scale model. *Physics of Fluids*, 6(12):4057–4059, 1994.

[29] J. Smagorinsky. General circulation experiments with the primitive equations. I. The basic experiment. *Mon. Wea. Rev.*, 91(3):99–164, 1963.

[30] T. W. Leland and P. S. Chappelear. The corresponding states principle. A review of current theory and practice. *Industrial and Engineering Chemistry Fundamentals*, 60(7):15–43, 1968.

[31] J. S. Rowlinson and I. D. Watson. The prediction of the thermodynamic properties of fluids and fluid mixtures–I. The principle of corresponding states and its extensions. *Chemical Engineering Science*, 24(8):1565–1574, 1969.

[32] R. C. Reid, J. M. Prausnitz, and B. E. Polling. *The Properties of Liquids and Gases*. McGraw-Hill, New York, New York, 4th edition, 1987.

[33] G. J. VanWylen and R. E. Sonntag. *Fundamentals of Classical Thermodynamics*. John Wiley and Sons, Incorporated, New York, New York, 3rd edition, 1986.

[34] S. Gordon and B. J. McBride. Computer program for calculation of complex chemical equilibrium compositions, rocket performance, incident and reflected shocks and Chapman-Jouguet detonations. Technical Report NASA SP-273, National Aeronautics and Space Administration, 1971.

[35] R. J. Kee, F. M. Rupley, and J. A. Miller. Chemkin thermodynamic data base. Technical Report SAND87-8215B, Sandia National Laboratories, 1990. Supersedes SAND87-8215 dated April 1987.

[36] J. F. Ely and H. J. M. Hanley. Prediction of transport properties. 1. Viscosity of fluids and mixtures. *Industrial and Engineering Chemistry Fundamentals*, 20(4):323–332, 1981.

[37] J. F. Ely and H. J. M. Hanley. Prediction of transport properties. 2. Thermal conductivity of pure fluids and mixtures. *Industrial and Engineering Chemistry Fundamentals*, 22(1):90–97, 1981.

[38] R. B. Bird, W. E. Stewart, and E. N. Lightfoot. *Transport Phenomena*. John Wiley and Sons, Incorporated, New York, New York, 1960.

[39] J. O. Hirschfelder, C. F. Curtiss, and R. B. Bird. *Molecular Theory of Gases and Liquids*. John Wiley and Sons, Incorporated, New York, New York, 2nd edition, 1964.

[40] S. Takahashi. Preparation of a generalized chart for the diffusion coefficients of gases at high pressures. *Journal of Chemical Engineering of Japan*, 7(6):417–420, 1974.

[41] N. B. Vargaftik. *Tables on the Thermophysical Properties of Liquids and Gases*. John Wiley and Sons, Incorporated, New York, New York, 2nd edition, 1975.